PCCP

Accepted Manuscript

ROYAL SOCIETY OF CHEMISTRY

www.rsc.org/pccp

Journal Name

ARTICLE

Electron Transport Mechanism of Bathocuproine Exciton Blocking Layer in Organic Photovoltaics

Received 00th January 20xx,
Accepted 00th January 20xx

DOI: 10.1039/x0xx00000x

www.rsc.org/

Jeihyun Lee [a,†], Soohyung Park [a,†], Younjoo Lee [a], Hyein Kim [a], Dongguen Shin [a], Junkyeong Jeong [a], Kwangho Jeong [a], Sang Wan Cho[b], Hyunbok Lee[c,*] and Yeonjin Yi[a,*]

Efficient exciton management is a key issue to improve the power conversion efficiency of organic photovoltaics (OPVs). It is well known that the insertion of an exciton blocking layer (ExBL) having a large band gap promotes the efficient dissociation of photogenerated excitons at the donor-acceptor interface. However, the large band gap induces an energy barrier which disrupts the charge transport. Therefore, building an adequate strategy based on a knowledge of the true charge transport mechanism is necessary. In this study, the true electron transport mechanism of a bathocuproine (BCP) ExBL in OPVs is comprehensively investigated by in situ ultraviolet photoemission spectroscopy, inverse photoemission spectroscopy, density functional theory calculation, and impedance spectroscopy. The chemical interaction between deposited Al and BCP induces new states within the band gap of BCP, so that electrons can transport through these new energy levels. Localized trap states are also formed upon the Al-BCP interaction. The activation energy of these traps is estimated with temperature-dependent conductance measurements to be 0.20 eV. The Al-BCP interaction induces both transport and trap level in the energy gap of BCP and their interplay results in the electron transport observed.

Introduction

The short exciton diffusion length of a photoactive layer (~10 nm) in organic photovoltaics (OPVs) is one of the inveterate problems limiting the power conversion efficiency (PCE). In small molecule OPVs, which are comprised of a multilayered structure, it is well known that the insertion of an exciton blocking layer (ExBL) having a large band gap improves the PCE significantly by conveying the excitons to the interface of a donor and an acceptor. The requirements for efficient ExBLs are: (1) a larger band gap than photoactive layer which blocks the excitons but does not dissociate them, and (2) no charge injection barrier from a photoactive layer to an ExBL.

Bathocuproine (BCP) is a widely used ExBL between a cathode and an acceptor in OPVs[1,2] due to its superior properties of exciton blocking and electron extraction.[3-5] Its large energy gap[6,7] allows blocking of the excitons generated in the active layer, and thus the PCE is improved significantly by preventing exciton quenching at the interface of the cathode/acceptor.[3] However, in view of electron transport, the electron extraction barrier at the interface of cathode/BCP/acceptor (e.g. Al/BCP/C_{60}) increases, making it difficult to extract electrons from the acceptor to the cathode due to the low electron affinity (EA) of BCP.[8,9] Nevertheless, good contact through BCP has been reported with enhanced current density.[5,10-13] To explain this conflict, electron conduction through the cathode metal-induced defect states has been suggested and is currently believed to be the electron transport mechanism in the BCP ExBL.[10] However, the defect states responsible for the electron conduction are not trivial: generally "defect" states act as electron traps when the traps are far from the transport level, which is contrary to the enhanced electron conduction. In this regard, the origin of electron transport enhancement is not clear. Particularly, direct observation of the unoccupied defect or gap states that can convey electrons, is absent.

To determine the transport levels of BCP, the electronic structures of the Al/BCP interface has been studied and interfacial gap states have been reported.[14-17] In addition, Nakayama *et al.* reported another gap state at the BCP/C_{60} interface.[18] However, in these studies, only occupied gap states below the Fermi level (E_F) were measured, which are not an associated level for electron transport directly. For good electron transport, there should be sufficient density of unoccupied states near the E_F. Apart from this, metal-BCP interactions would generate some imperfection in the BCP ExBL and that should act as a trap site as well. The interplay between these transport and trap levels would result in the electron conduction observed with a BCP ExBL. To understand the true electron transport mechanism of BCP, both transport and trap levels should be analyzed simultaneously.

In this study, we comprehensively analyzed the electron transport mechanism by probing the transport and trap levels

[a] Institute of Physics and Applied Physics, Yonsei University, 50 Yonsei-ro, Seodaemoon-Gu, Seoul, 03722, South Korea. *E-mail:yeonjin@yonsei.ac.kr
[b] Department of Physics, Yonsei University, 1 Yonseidae-gil, Wonju-si, Gangwon-do, 26493, South Korea.
[c] Department of Physics, Kangwon National University, 1 Gangwondaehak-gil, Chuncheon-si, Gangwon-do, 24341, South Korea. *E-mail: hyunbok@kangwon.ac.kr
† Both authors contributed equally to this work.

using *in situ* ultraviolet photoemission spectroscopy (UPS) and inverse photoemission spectroscopy (IPES), theoretical model, temperature-dependent current density-voltage (*J-V*) characteristics and impedance spectroscopy (IS). UPS and IPES measurements showed the density of gap states both below and above the E_F in the BCP layer upon Al deposition. The density of gap states was also reproduced well with the theoretical model. The density of gap states above the E_F could provide an electron transport path for the current enhancement. Furthermore, trap levels due to the defect formation in addition to the transport level were estimated with IS measurements. Combining these results, the true electron transport mechanism of the BCP layer was discussed.

Results and discussion

A. UPS and IPES measurements

UPS measurements were carried out to investigate the electronic structures of Al/BCP/C_{60}. ITO was used as a substrate and a 10 nm-thick C_{60} layer was deposited on it as an acceptor in OPVs. Then, BCP (0.3, 0.7, 1.5, 3.0, 6.0 and 10.0 nm) and Al (0.02, 0.05, 0.1, 0.2, 2.0 and 5.0 nm) were deposited on C_{60} in a stepwise manner**. Figure 1a** shows the secondary electron cutoff (SEC) region during the deposition. The initial work function (Ψ) of 10 nm-thick C_{60} is 4.39 eV. The SEC shifts by 0.99 eV toward the high binding energy side during the step-by-step deposition of BCP on C_{60}. It shifts further by 0.35 eV with the Al deposition up to 0.1 nm. Depositing more Al, it moves back toward lower binding energies by 0.91 eV, which approaches the Ψ of Al metal (3.96 eV at 5 nm-thick). The HOMO region spectra during the deposition are shown in **Figure 1b**. The 10 nm-thick C_{60} shows clear HOMO emission features with its onset at 2.08 eV below the E_F. With the BCP deposition, its characteristic emission features emerge gradually and its HOMO onset is seen at 2.93 eV at the 10 nm-deposition step. During BCP deposition, both the C_{60} and BCP HOMO onsets shift toward higher binding energies. However, it is difficult to determine the exact magnitude of shifts due to the spectral overlap between C_{60} and BCP. Thus the spectra were deconvoluted with the pristine spectrum of both C_{60} and BCP taken from the initial C_{60} and bulk (10 nm-thick) BCP spectrum. As a result, the HOMO shift of C_{60} and BCP was evaluated to be 0.30 and 0.83 eV, respectively. These two energy level shifts are directly related the band bending (V_b) of an organic layer. Since the energy level shift of an overlayer measured by photoemission spectroscopy contains the substrate V_b, we subtracted the C_{60} shift from the total shift.[19] Thus, the V_b of C_{60} and BCP layers is 0.30 and 0.53 eV. These shifts are due to the polarization of charge densities at interface between BCP and C_{60}.[20,21] No gap state was observed at this BCP/C_{60} interface, which is due to its low density of states (DOS) that could be observed with low energy UPS measurements.[18] On the other hand, as Al is deposited on a BCP layer, gap states emerge at the first deposition step as shown in the square region with purple color.

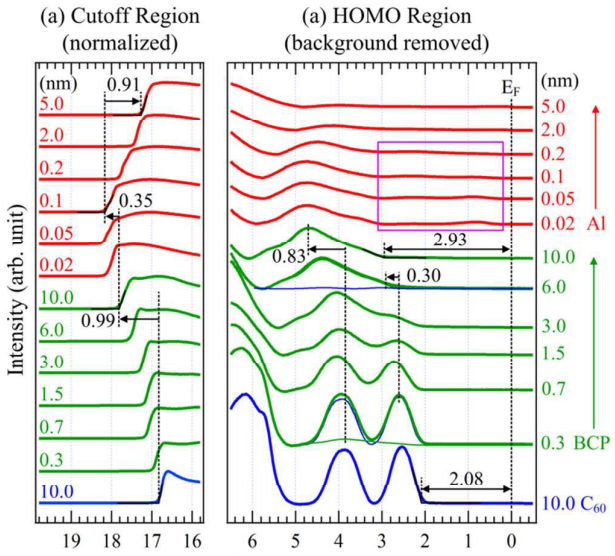

Figure 1. UPS spectra of Al/BCP/C_{60}. (a) Secondary electron cutoff and (b) HOMO region are presented with peak deconvolution.

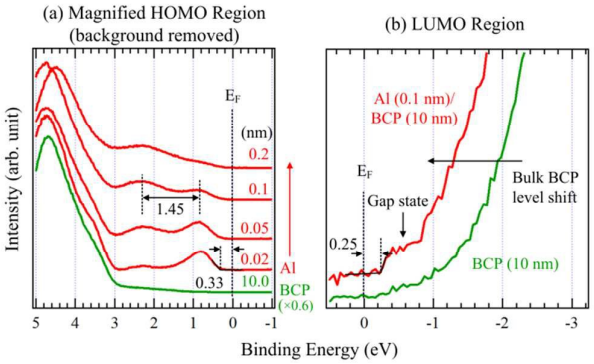

Figure 2. (a) Magnified HOMO region of Al (0.02, 0.05, 0.1 and 0.2 nm) on BCP (10 nm) clearly shows gap states. (b) Unoccupied states of BCP (5 nm) and Al (0.05 nm)/BCP (5 nm) measured by IPES. It shows clear increases in spectral features within the original band gap.

To examine the electronic properties of gap states in detail, the spectra were magnified and shown in **Figure 2a**. Two distinct peaks are observed: one is at 0.33 eV below the E_F and the other is distant from it by 1.45 eV. Such gap states would be formed at not only the occupied states but also the unoccupied states. While the occupied gap state can assist the hole conduction,[22,23] the unoccupied gap state would contribute to the electron conduction.[24] Therefore, the direct confirmation of the unoccupied gap state is indispensable to understanding the electron transport, but there has been no direct evidence for the unoccupied gap state of Al/BCP. To confirm the formation of unoccupied gap states upon Al deposition, IPES measurements were performed on pristine and Al-deposited BCP (**Figure 2b**). The 10 nm-thick BCP was prepared on an ITO substrate and IPES measurements were conducted. Next, the 0.1 nm-thick Al was deposited on BCP to see the emergence of unoccupied gap states. From the IPES spectra, new emission features at 0.25 eV with respect to the E_F, are seen.[25] These new emission features are attributed to

the gap states from the interaction between BCP and Al. The bulk characteristic emission of Al can be excluded due to the thin Al thickness (0.1 nm). In addition to the gap state formation, the bulk BCP LUMO level is also shifted toward lower binding energies due to the weak n-type doping effect by the metal-organic interaction (Al-BCP).[26] The value would refer to the SEC shift (0.35 eV) as shown in Figure 1a. Thus the emergence of unoccupied gap states along with the occupied gap states is confirmed. Previous reports found that a cathode metal, such as Ag and Al, diffuses about 10 nm into a BCP layer during its deposition.[10,12,27] Thus the gap states could exist within a 10 nm depth of BCP, which is a typical optimum thickness of a BCP ExBL in OPVs.

B. Theoretical study

To verify the origin of the gap state formation, density functional theory (DFT) calculations were performed for BCP and the Al-BCP complex. A model of metal-organic complex formation was adopted since it describes the DOS measured well.[24,28,29] The DOS of a BCP single molecule was calculated with C_2 symmetry.[30] The result is depicted in **Figure 3a**. The upper spectrum is the measured UPS and IPES spectra of 10 nm-thick BCP. The vertical bars indicate the discrete molecular levels and the lower spectrum is the simulated DOS. The measured DOS and simulated occupied DOS are in good agreement, although gas phase molecules were used for DFT calculations. This is due to the weak intermolecular interactions of the van der Waals type among organic molecules, which renders minimal solid state effects.[31-33] When compared between measured and simulated unoccupied DOS, the IPES spectrum is much broader than the simulated DOS. By taking into account the resolution of IPES, the measured and simulated results are well matched. From the UPS and IPES measurements, the transport gap of 4.70 eV for BCP is observed, which is higher than the optical gap of 3.50 eV[34] reported and similar to the transport gap in literature.[6,7]

To investigate the interaction mechanism between Al and BCP, a single Al atom was attached to the BCP with various geometries. Several initial geometries were modeled and their geometries were fully relaxed to meet energetic minima. Among the resulting geometries, Al interacting with two N in phenanthroline (inset in **Figure 3b**) shows the lowest total energy and gives gap states as observed in the measured DOS. This interaction is due to the free energy minimization during the Al deposition process on BCP. During the Al deposition, some Al atoms interact directly with the surface BCP, and others diffuse into the BCP layer and interact somewhere within 10 nm depth. It is believed that these processes are possible due to the thermal energy obtained during the evaporation process. These Al atoms have high chance to bond with N atoms of BCP because the enthalpy reduction is maximum among possible interaction sites. The enthalpy change (ΔH) could be obtained from our DFT calculations as follows:

$$\mathrm{Al} + \mathrm{BCP} \rightarrow (\mathrm{Al} - \mathrm{BCP})_{\mathrm{complex}} + \Delta\mathrm{H}$$

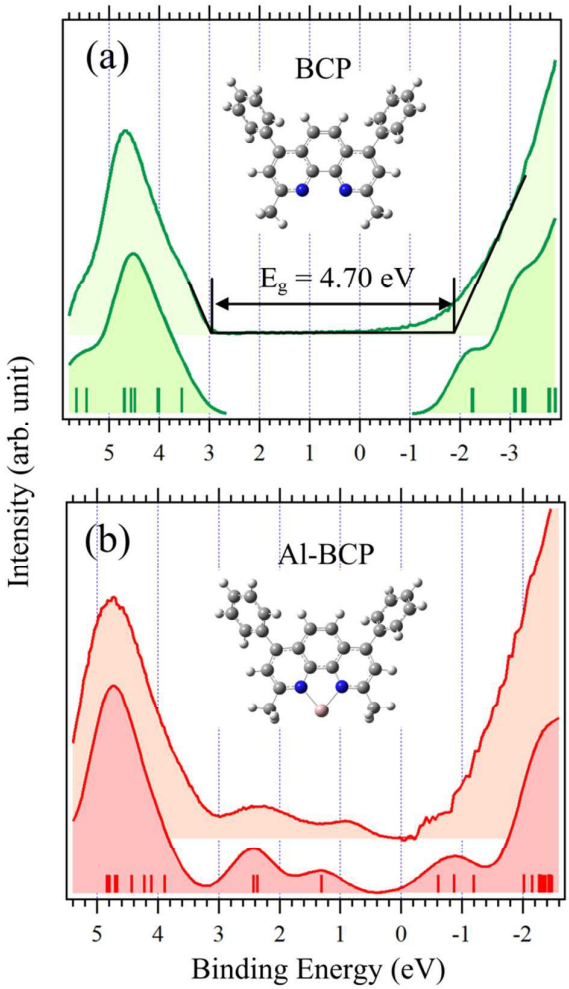

Figure 3. Simulated DOS (lower spectrum) and measured UPS and IPES spectra (upper spectrum) of (a) BCP and (b) Al-BCP complex. Insets show the theoretical models used for DFT calculations. Bars in the Figures are Kohn-Sham energy and the simulated DOS is generated by converting Kohn-Sham energy with a Gaussian function having a width of 0.5 eV. (Atomic color code: gray for C, blue for N, pink for Al, white for H).

, and the ΔH was estimated to be 241.848 kJ/mol, indicating the exothermic reaction. This is the driving force for the Al-BCP chemical interaction.

The simulated DOS of the Al-BCP complex is depicted in Figure 3b (lower spectrum). With the Al interaction, two new states emerge below the E_F, which corresponds well to the UPS spectrum (upper spectra, 0.1 nm Al deposition step taken from Figure 2a) with gap states. More important to note are the changes in the unoccupied levels which are associated with electron transport. With the formation of the Al-BCP complex, unoccupied gap states emerge above the E_F. There are three unoccupied molecular levels very close to the E_F in the simulated DOS, which are responsible for the increased spectral features in the IPES spectrum with Al deposition. This indicates that there are enough unoccupied DOS near E_F for electron transport. In addition, the origin of the gap state is the Al-BCP complex formation.[14] The unoccupied gap states

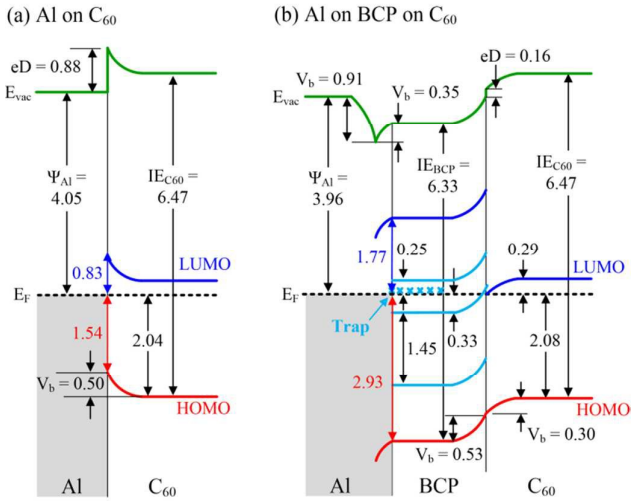

Figure 4. Energy level diagrams of (a) Al/C_{60} and (b) Al/BCP/C_{60}. E_F the Fermi level, E_{vac} the vacuum level, V_b the band bending, eD the interface dipole and Ψ_{Al} the work function of Al are indicated. (unit: eV)

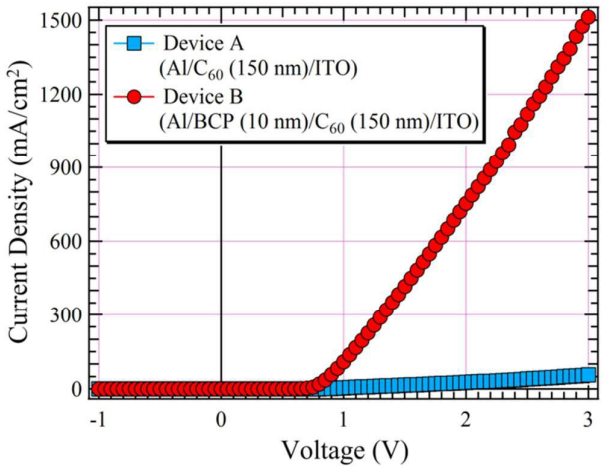

Figure 5. Measured current density-voltage characteristics of electron-only devices with (Device B) and without (Device A) BCP layer at 300 K.

should act as a transport level from C_{60} to the Al cathode since the BCP LUMO is energetically too far to accept electrons. From the well-matched theoretical results with the UPS and IPES measurements, the formation of the Al-BCP complex giving occupied and unoccupied gap states in the original band gap of BCP is confirmed.

C. Energy level diagrams

Combining all the information obtained from the UPS/IPES measurements, complete energy level diagrams of Al/C_{60} and Al/BCP/C_{60} are illustrated in **Figure 4a** and **4b**, respectively. The measured ionization energy (IE) of C_{60} and BCP is 6.47 eV and 6.33 eV, which agrees well with previous reports.[8,9] The LUMO level of C_{60} was estimated from the reported transport gap of 2.37 eV,[35] and that of BCP was estimated from the measured transport gap of 4.70 eV. To compare the changes of electronic structures by inserting BCP between Al and C_{60}, UPS measurements for Al/C_{60} were also conducted with step-by-step deposition of Al on the 10 nm-thick C_{60}. The pristine HOMO level of the 10 nm-thick C_{60} is located at 2.04 eV below the E_F. During Al deposition on C_{60}, the V_b of 0.50 eV and eD of 0.88 eV are established and the LUMO-E_F offset (Φ_e) is 0.83 eV. Continuing Al deposition, the Al bulk work function of 4.05 eV is achieved.

The energy level alignment of Al/BCP/C_{60} is shown in Figure 4b. When a 10 nm-thick BCP layer is deposited on C_{60}, an interface dipole (eD) of 0.16 eV at the interface of BCP/C_{60} and V_b of 0.53 eV in a BCP layer are induced. This large band bending (V_b) is due to the strong polarization effect of C_{60} in combination with the giant surface potential of BCP.[9,18,36] Combining the measured transport gap and the HOMO position of the 10 nm-thick BCP (2.93 eV), the Φ_e at the interface of Al/BCP is 1.77 eV, which is larger than that of Al/C_{60}. This increased Φ_e contrasts with the enhanced electron collection in OPVs.

Therefore, the unoccupied gap states should be noted. First, the LUMO level of C_{60} side shows a downward shift (V_b = 0.30 eV) as the BCP layer is deposited, and thus it is very close to the E_F. The most dramatic changes occur with Al deposition on BCP: unoccupied gap states near the E_F due to the Al diffusion.[10,12,27] These unoccupied gap sates are very close to the C_{60} LUMO level and the E_F, providing an efficient electron transport path. This would contribute to the current enhancement. Further Al deposition induces the V_b of 0.35 eV at the Al/BCP interface and the work function approaches the bulk Al. Collectively, electrons in the C_{60} LUMO can easily pass through the unoccupied gap states above the E_F in BCP.

D. *J-V* measurements

To verify the role of unoccupied gap states as an electron transport path, *J-V* measurements were conducted for Device A: Al/C_{60} (150 nm)/ITO and Device B: Al/BCP (10 nm)/C_{60} (150 nm)/ITO. In these measurements, Al and ITO were used as a cathode and an anode and thus devices are electron-dominated (electron-only device). **Figure 5** shows the measured *J-V* characteristics of devices at 300 K. Much enhanced *J* is observed in Device B compared with Device A at the forward bias region as expected from the previous section. Since intrinsic free carriers are lacking in organic semiconductors, the current observed is due to the injection from the Al cathode over the Φ_e. As shown in Figure 4, the BCP LUMO cannot be the electron transport level in Al/BCP/C_{60} structure since the Φ_e at Al/BCP is 1.57 eV which is much higher than that of Device A (0.83 eV), and thus it cannot improve *J-V* characteristics. This confirms again that the unoccupied gap states are the culprit for the electron transport. To understand underlying conduction mechanism of a BCP layer, we measured temperature-dependent *J-V* characteristics of Device A (w/o BCP) and B (w/ BCP). As shown in **Figure 6**, Device A does not show the slope change in log *J*-log *V* plot at the low bias regime (< ~0.7 V) by temperature variations, while Device B does strongly. In addition, *J* of device B decreases greatly as the temperature decreases (more than

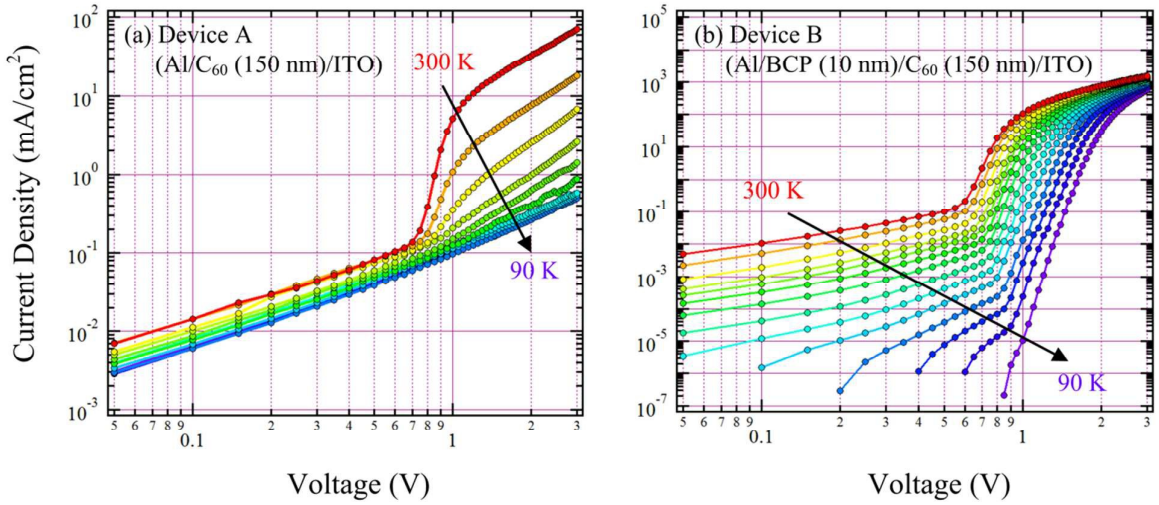

Figure 6. Measured current density-voltage characteristics of electron-only devices with (Device B) and without (Device A) a BCP layer by changing the temperature (From 300 K to 90 K).

four orders of magnitude). This temperature dependency is related to the thermal carrier activated from the trap states in BCP.

E. IS measurements

Previous studies suggested that localized trap states with various origins exist in organic molecular solids.[37] Al diffusion into a BCP layer must generate various defect states, *e.g.,* structural defects and chemical impurities,[37] which hinder electron transport, while simultaneously creating a transport path by forming the unoccupied gap states. Generally, the density of trap levels is too small to be detected by conventional UPS measurements but could play a crucial role in carrier transport. Thus, it is important to understand the trap level, and IS measurements can detect such levels.[10,38]

Figure 7a and **7b** show the impedance modulus ($|Z|$) and phase angle (ϕ) of Device A and B as a function of applied ac frequency (f) at V_{dc} = 0 V (*dc* bias at the device) measured at 300 and 90 K. In Figure 6a, a transition from f-independent to f-dependent $|Z|$ at 600 Hz is seen except Device B measured at 90 K. Basically, all devices have a resistive (R) and capacitive (C) component and their behaviors can be understood qualitatively with simple parallel RC circuit. Since the impedance of a parallel RC circuit is $Z = [1/R + j(2\pi f)C]^{-1}$, the measured impedance approaches R and $1/j(2\pi f)C$ at low and high frequency regimes, respectively. Therefore, the pure resistive characteristics at low frequencies emerge as the frequency-independent $|Z|$ in Figure 7a. However, Device B at 90 K does not show the frequency-independent behavior at low frequency. This means that R is very large at low temperature and thus the $1/j(2\pi f)C$ dominates the $|Z|$ even at the low f regime. Conversely, at the high f regime, $1/j\ (2\pi f)\ C$ dominates $|Z|$, where C is the geometric capacitance of the Devices A and B. Since the Devices A and B have the same geometry, they show identical $|Z|$ at the high f regime even at different temperatures. All spectra are overlapped above 10^3 Hz with pure capacitive characteristics with $|Z| = 1/(2\pi f)C$.[39] The significant R increase of Device B at 90 K originates from the BCP interlayer because Device A shows the constant $|Z|$ at any temperature in the low f region. In Figure 7b, Device B again clearly shows the pure capacitive characteristics (constant φ of -90°) at 90 K for the 10-10^5 Hz range while, at 300 K, it shows the pure resistive characteristics (φ of zero) at low f and the φ increases gradually to -90°. This implies a conductance reduction of Device B at low temperature. This temperature-dependent conductance of Device B would be due to the thermally activated carriers from the trap states in BCP. With Al deposition on BCP, diffused Al makes (1) the large density of gap states as seen in UPS and IPES spectra due to the Al-BCP complex formation and (2) the structural defects and chemical impurities in a BCP layer. These defect/impurity sites would act as the localized trap levels below the transport levels of BCP (i.e. the unoccupied gap states as aforementioned). Therefore, elect rons would be trapped at such trap levels inside the BCP layer. At room temperature and a low f (~dc) regime, trapped electrons can be excited to the transport levels (the unoccupied gap states) from the trap levels and can contribute to the conductance with trap-detrap processes (Device B at 300 K). However, at low temperature, the thermal energy is not enough to excite the trapped electrons, and thus the conductance decreases. This is the main origin for Device B showing larger |Z| (Figure 7a) with pure capacitive characteristics at 90 K (Figure 7b). When the f is increased, both trapped and mobile electrons cannot respond to the external ac electric field instantaneously, and thus all devices show pure capacitor characteristics and the φ reaches to -90° at the 10^4~10^5 Hz range. In this high f condition, electronic and atomic polarization of C_{60} and BCP can occur.[40] The same is true for the $|Z|$-f characteristics seen as the frequency-dependent $|Z|$ decreases above 10^3 Hz. The abrupt phase decrease down to below 0° for >10^6 Hz is not related to the

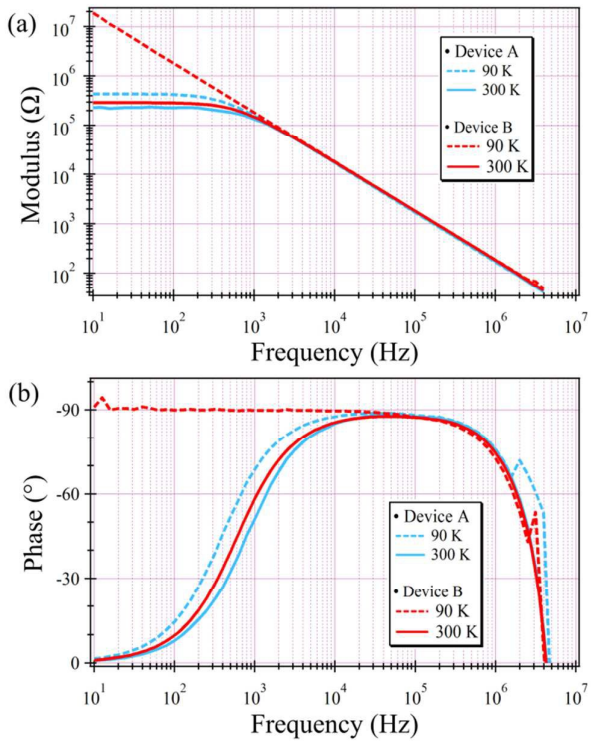

Figure 7. (a) Z-*f* and (b) *ϕ*-*f* characteristics of Device A and B at 300K and 90 K with the relation of $\boldsymbol{Z} = |Z|e^{i\phi}$.

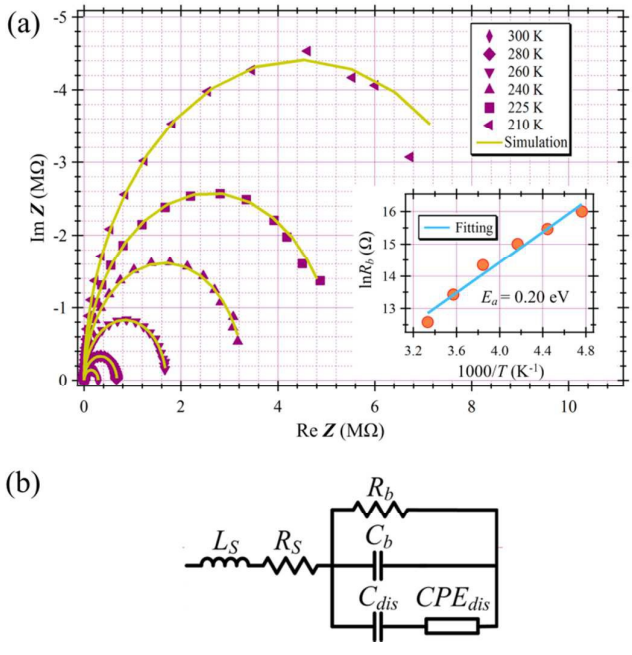

Figure 8. (a) Nyquist plot of Device B at 300, 280, 260, 240, 225 and 210 K and (b) equivalent circuit for simulation. Simulation results are also indicated with solid lines. Inset shows lnR_b versus 1000/T relation, where R_b is extracted from the simulation and each value is presented in Table 1.

Table 1. Equivalent circuit parameters used to simulate the measured data as shown in Figure 8.

T [K]	R_s [Ω]	R_b [MΩ]	C_b [nF]	C_{dis} [10^{-4} F]	CPE_{dis} Q [x 10^{-9}]	CPE_{dis} n	L_s [μH][a)]
300	46.36	0.29	0.82	1.10	0.26	0.88	1.42
280	42.31	0.68	0.82	1.09	0.25	0.87	1.42
260	42.46	1.70	0.82	1.02	0.23	0.87	1.42
240	42.11	3.31	0.82	0.99	0.22	0.87	1.42
225	42.97	5.23	0.82	0.99	0.12	0.87	1.42
210	42.34	8.95	0.82	0.99	0.12	0.87	1.42

[a)] L_s was fixed during simulation due to the external parameter originated from measurement line

device itself. In this frequency region, device characteristics are negligible and the inductance of the equipment line (L_s) and probe-device contact resistance (R_s) are dominant.

Since the conduction in Device B is related to the both trap and transport levels (unoccupied gap states) in BCP, the activation energy (E_a) from the trap levels to the transport levels is estimated with the Arrhenius relation: The bulk resistance R_b, which reflects the conductance of the device at given temperature T, has an inverse relation of $R_b = R_0 \exp(E_a/k_BT)$, where R_0 is a constant, k_B is the Boltzmann constant and T is the temperature.[41,42] To get the R_b of Device B, IS spectra were measured with temperature variation from 300 to 210 K and shown in **Figure 8a** as the Nyquist plot. In addition, an equivalent circuit was constructed and fitted with the measured data to extract physical properties inside the devices.[43,44] This is depicted in **Figure 8b**, where L_s is the inductance of the equipment line, R_s is the contact resistance between the electrodes and probes, R_b is the bulk resistance, C_b is the bulk capacitance (or geometric capacitance), and C_{dis} and CPE_{dis} describe dispersive characteristics of charge transport.[45] (Detailed fitting parameters are shown in **Table 1**.) The simulation reproduces the measured IS data nicely as shown in Figure 8a. From the well-matched simulation results, R_b was extracted and the (lnR_b)-(1000/T) relation is depicted in the inset of Figure 8a. Linear fitting gives E_a as the slop of the line and 0.20 eV was obtained. E_a is the energetic difference between the transport (E_{trans}) and trap (E_{trap}) levels in an average manner.[38] That is, the trap levels are located 0.20 eV below the transport levels.

Collectively, schematics of electron transport mechanisms including transport and trap levels in BCP are depicted in **Figure 9**. Trap energy levels are represented with dispersive structures due to the disordered nature of organic films. Electrons from the C_{60} LUMO are transported to the Al electrode through the unoccupied gap states in BCP with trap-detrap processes. The trap levels are 0.20 eV below the transport level in an average manner. The average energetic position of trap state displayed in Figure 4b as marker X. Electrons in C_{60} from exciton dissociation cannot transfer to the BCP LUMO due to the high injection barrier. However, the unoccupied gap state originates from Al-BCP complex provides efficient electron transport path. Electrons in a BCP layer are

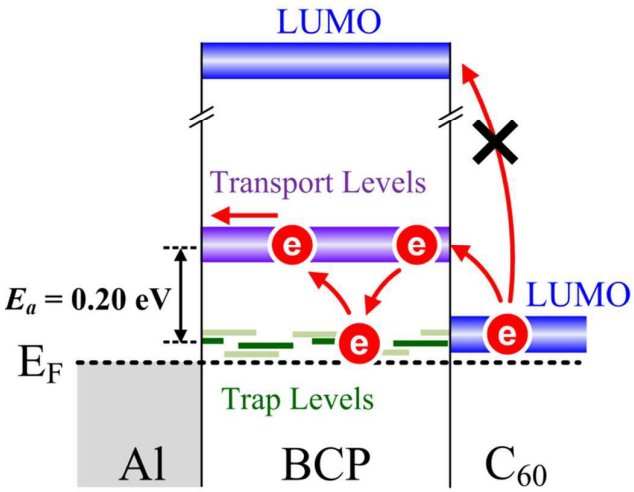

Figure 1. Electron transport mechanism of BCP including transport states and trap states.

transferred by trap-detrap process, and they are collected to the Al cathode.

Conclusions

The electron transport mechanism of BCP was investigated with an Al/BCP/C_{60} structure. Al interaction with BCP produces both occupied and unoccupied gap states in the pristine band gap of BCP. These unoccupied gap states provide the electron transport paths. The origin of the gap states is the formation of the Al-BCP complex, which was modeled from theoretical calculations showing excellent agreement with measured UPS and IPES spectra. The temperature-dependent *J-V* characteristics of electron-only devices confirms substantial improvement in electron transport with BCP and thus it is verified that unoccupied gap states act as the electron transport level of BCP. In addition, IS measurements indicate that Al interactions with BCP produce not only transport level but also trap levels in the band gap. The activation energy of these trap states was estimated as 0.20 eV by the temperature-dependent conductance measurements. Therefore, the interplay of trap-detrap processes between transport levels and trap levels is the true electron transport mechanism in OPVs.

Experimental

A. Ultraviolet photoemission spectroscopy (UPS)

Measurements were carried out using a PHI 5700 spectrometer and ultraviolet (He I, 21.22 eV) light sources to investigate the electronic structures of Al/C_{60} and Al/BCP/C_{60}. ITO coated glass was used as a substrate, cleaned with solvents[46] for 15 min and UV-ozone treated for 30 min, respectively, to remove the contamination on the surface. C_{60} (SES research, 99.9%), BCP (Jilim OLED Material Tech, 99%) and Al were thermally evaporated at the rate of 0.01 nm/s in the deposition chamber. *In situ* UPS measurements were conducted without breaking the vacuum between deposition and measurement with a stepwise manner. The base pressure of the deposition and analysis chambers were 1.0×10^{-8} and 6.0×10^{-9} Torr, respectively. During measurement, a -10 V was applied to the sample to obtain the true SEC.

B. Inverse photoemission spectroscopy (IPES)

IPES measurements were carried out by using a low energy electron gun with a BaO cathode. To detect the emitted photons a band pass filter of 9.5 eV in isochromat mode was adopted. The 10 nm-thick BCP was deposited on an ITO substrate and UPS measurements were conducted without breaking the vacuum. After checking the identical spectrum of BCP, it was transferred to the analysis chamber with the ultrahigh vacuum carrier and measurements were performed. Then 0.1 nm-thick Al was deposited on BCP in the deposition chamber which was directly connected to the IPES analysis chamber. Finally, IPES measurements were performed by transferring the sample to the analysis chamber without breaking the vacuum.

C. Theoretical calculation

Theoretical calculations using DFT were performed on a single molecule of BCP and an Al-BCP complex. A Becke-style 3 parameters exchange and Lee–Yang–Parr correlation functional (B3LYP)[47-49] and a 6-31+G(d) basis set were used in geometry optimization and single point energy calculations implemented in the Gaussian 09 package.[50] To compare between theoretical calculations and measured UPS and IPES spectra, occupied and unoccupied states regions of simulated DOS were rigidly shifted to match the onset of UPS and IPES, respectively.

D. Current density-voltage (J-V) characteristics and impedance spectroscopy (IS) measurements

J-V characteristics and IS measurements were carried out with a Keithley 2400 source-measure unit and a Solartron 1260 impedance/gain-phase analyzer, respectively. Electron-only devices which consisted of Al (100 nm)/BCP (0 or 10 nm)/C_{60} (150 nm)/ITO were fabricated by thermal evaporation using a shadow mask (the active area of the device was 2 mm × 2 mm) in an ultrahigh vacuum chamber. Measurements were performed on the Linkam stage to vary the device temperature from 300 to 90 K with the base pressure at 10^{-2} Torr. The temperature was controlled by a liquid nitrogen cooling system and its variation was carefully controlled by Linksys 32 software. Frequencies from 10-10^7 Hz at an oscillation voltage of 25 mV were adopted during IS measurements.

E. Film thickness

The film thicknesses were monitored by a quartz crystal microbalance which was calibrated via a cross-sectional SEM (JEOL-6700F) and surface profiler (Alpha-step 500 Surface Profiler).

Acknowledgements

This work was supported by the National Research Foundation of Korea (Grant No. 2015R1C1A1A01055026, 2013R1A1A1004778 and 2012M3A7B4049801), Samsung Display Company, the Yonsei University Future-leading Research Initiative of 2014 (2014-22-0123) and Defense Acquisition Program Administration (DAPA) and the Agency for Defense Development (ADD).

Note and references

1 Chang, C.-C., Lin, C.-F., Chiou, J.-M., Ho, T.-H., Tai, Y., Lee, J.-H., Chen, Y.-F., Wang, J.-K., Chen, L.-C., Chen, K.-H., *Appl. Phys. Lett.* 2010, *96*, 263506.
2 Zou, Y., Holst, J., Zhang, Y., Holmes, R. J., *J. Mater. Chem. A* 2014, *2*, 12397.
3 Peumans, P., Bulović, V., Forrest, S. R., *Appl. Phys. Lett.* 2000, *76*, 2650.
4 Heutz, S., Sullivan, P., Sanderson, B. M., Schultes, S. M., Jones, T. S., *Sol. Energy Mater. Sol. Cells* 2004, *83*, 229.
5 Gommans, H., Verreet, B., Rand, B. P., Muller, R., Poortmans, J., Heremans, P., Genoe, J. *Adv. Funct. Mater.* 2008, *18*, 3686.
6 Kahn, A., Koch, N., Gao, W., *J. Polym. Sci. Pt. B-Polym. Phys.* 2003, *41*, 2529.
7 Gao, W., Kahn, A., *Appl. Phys. Lett.* 2003, *82*, 4815.
8 Tang, J. X., Zhou, Y. C., Liu, Z. T., Lee, C. S., Lee, S. T., *Appl. Phys. Lett.* 2008, *93*, 043512.
9 Akaike, K., Kubozono, Y., *Org. Electron.* 2013, *14*, 1.
10 Peumans, P., Forrest, S. R., *Appl. Phys. Lett.* 2001, *79*, 126.
11 Luo, D. Y., Yu, L. M., Man, J. X., Liu, T. L., Li, J. J., Xu, T., Liu, Z., Wang, Z. B., Lu, Z. H. A, *J. Appl. Phys.* 2013, *113*, 224506.
12 Huang, J., Yu, J., Lin, H., Jiang, Y., *J. Appl. Phys.* 2009, *105*, 073105.
13 Vogel, M., Doka, S., Breyer, C., Lux-Steiner, M. C., Fostiropoulos, K., *Appl. Phys. Lett.* 2006, *89*, 163501.
14 Wang, S., Sakurai, T., Hao, X., Fu, W., Masuda, S., Akimoto, K., *J. Appl. Phys.* 2013, *114*, 183707.
15 Sakurai, T., Toyoshima, S., Kitazume, H., Masuda, S., Kato, H., Akimoto, K., *J. Appl. Phys.* 2010, *107*, 043707.
16 Masuda, S., *Appl. Surf. Sci.* 2010, *256*, 4054.
17 Aoki, M., Toyoshima, S., Kamada, T., Sogo, M., Masuda, S., Sakurai, T., Akimoto, K., *J. Appl. Phys.* 2009, *106*, 043715.
18 Nakayama, Y., Nguyen, T. L., Ozawa, Y., Machida, S. i., Sato, T., Tokairin, H., Noguchi, Y., Ishii, H., *Adv. Energy Mater.* 2014, *4*, 1301354.
19 Schlaf, R., Parkinson, B. A., Lee, P. A., Nebesny, K. W., Armstrong, N. R., *J. Phys. Chem. B* 1999, *103*, 2984.
20 Vázquez, H., Gao, W., Flores, F., Kahn, A., *Phys. Rev. B* 2005, *71*, 041306.
21 Kahn, A., Zhao, W., Gao, W., Vázquez, H., Flores, F., *Chem. Phys.* 2006, *325*, 129.
22 Jeon, P., Lee, H., Lee, J., Jeong, K., Lee, J. W., Yi, Y., *Appl. Phys. Lett.* 2011, *99*, 073305.
23 Yi, Y., Jeon, P. E., Lee, H., Han, K., Kim, H. S., Jeong, K., Cho, S. W. *J., Chem. Phys.* 2009, *130*, 094704.
24 Yi, Y., Lee, Y. M., Park, Y., Kim, J. W., *Phys. Chem. Chem. Phys.* 2010, *12*, 9441.
25 Schedin, F., Thornton, G., Uhrberg, R. I. G., *Rev. Sci. Instrum.* 1997, *68*, 41.
26 Yan, L., Mason, M. G., Tang, C. W., Gao, Y., *Appl. Surf. Sci.* 2001, *175*, 412.
27 Rand, B. P., Li, J., Xue, J., Holmes, R. J., Thompson, M. E., Forrest, S. R., *Adv. Mater.* 2005, *17*, 2714.
28 Cho, S. W., Yi, Y., Seo, J. H., Kim, C. Y., Noh, M., Yoo, K.-H., Jeong, K., Whang, C.-N., *Synth. Met.* 2007, *157*, 160.
29 Lee, H., Cho, S. W., Lee, J., Jeon, P. E., Jeong, K., Lee, J. W., Yi, Y., *J. Appl. Phys.* 2012, *111*, 043712.
30 Gao, H., Qin, C., Zhang, H., Wu, S., Su, Z.-M., Wang, Y., *J. Phys. Chem. A* 2008, *112*, 9097.
31 Zahn, D. R. T., Gavrila, G. N., Salvan, G., *Chem. Rev.* 2007, *107*, 1161.
32 Lee, H., Lee, J., Jeong, K., Yi, Y., Lee, J. H., Kim, J. W., Cho, S. W., *J. Phys. Chem. C* 2012, *116*, 13210.
33 Lee, H., Lee, J., Park, S., Yi, Y., Cho, S. W., Kim, J. W., Kang, S. J., *Carbon* 2014, *71*, 268.
34 Hill, I. G., Kahn, A., *J. Appl. Phys.* 1999, *86*, 4516.
35 Yoshida, H., *J. Phys. Chem. C* 2014, *118*, 24377.
36 Noguchi, Y., Miyazaki, Y., Tanaka, Y., Sato, N., Nakayama, Y., Schmidt, T. D., Brütting, W., Ishii, H., *J. Appl. Phys.* 2012, *111*, 114508.
37 Kalb, W. L., Haas, S., Krellner, C., Mathis, T., Batlogg, B., *Phys. Rev. B* 2010, *81*, 155315.
38 Stallinga, P. *Electrical Characterization of Organic Electronic Materials and Devices*, Wiley, 2009.
39 Nau, S., Sax, S., List-Kratochvil, E. J. W., *Adv. Mater.* 2014, *26*, 2508.
40 Kao, K. C. *Dielectric Phenomena in Solids*, Elsevier Academic Press, 2004.
41 Hsieh, M.-T., Chang, C.-C., Chen, J.-F., Chen, C. H., *Appl. Phys. Lett.* 2006, *89*, 103510.
42 Atta, A. A., *J. Alloy. Compd.* 2009, *480*, 564.
43 Ecker, B., Egelhaaf, H.-J., Steim, R., Parisi, J., von Hauff, E., *J. Phys. Chem. C* 2012, *116*, 16333.
44 Ecker, B., Posdorfer, J., von Hauff, E., *Sol. Energy Mater. Sol. Cells* 2013, *116*, 176.
45 Cole, K. S., Cole, R. H., *J. Chem. Phys.* 1941, *9*, 341.
46 Lee, J., Lee, H., Jeon, P., Jeong, K., Kim, T. G., Kim, J. W., Yi, Y., *Appl. Phys. Lett.* 2012, *100*, 203301.
47 Becke, A. D., *J. Chem. Phys.* 1993, *98*, 5648.
48 Lee, C., Yang, W., Parr, R. G., *Phys. Rev. B* 1988, *37*, 785.
49 Sousa, S. F., Fernandes, P. A., Ramos, M. J., *J. Phys. Chem. A* 2007, *111*, 10439.
50 Frisch, M. J., Trucks, G. W., Schlegel, H. B., Scuseria, G. E., Robb, M. A., Cheeseman, J. R., Scalmani, G., Barone, V., Mennucci, B., Petersson, G. A., Nakatsuji, H., Caricato, M., Li, X., Hratchian, H. P., Izmaylov, A. F., Bloino, J., Zheng, G., Sonnenberg, J. L., Hada, M., Ehara, M., Toyota, K., Fukuda, R., Hasegawa, J., Ishida, M., Nakajima, T., Honda, Y., Kitao, O., Nakai, H., Vreven, T., Montgomery, J. A., Peralta, J. E. J., Ogliaro, F., Bearpark, M., Heyd, J. J., Brothers, E., Kudin, K. N., Staroverov, V. N., Kobayashi, R., Normand, J., Raghavachari, K., Rendell, A., Burant, J. C., Iyengar, S. S., Tomasi, J., Cossi, M., Rega, N., Millam, J. M., Klene, M., Knox, J. E., Cross, J. B., Bakken, V., Adamo, C., Jaramillo, J., Gomperts, R., Stratmann, R. E., Yazyev, O., Austin, A. J., Cammi, R., Pomelli, C., Ochterski, J. W., Martin, R. L., Morokuma, K., Zakrzewski, V. G., Voth, G. A., Salvador, P., Dannenberg, J. J., Dapprich, S., Daniels, A. D., Farkas, O., Foresman, J. B., Ortiz, J. V., Cioslowski, J., Fox, D. J. In *Gaussian 09*, Revision B.01 ed., Gaussian Inc.: Wallingford CT, 2009.

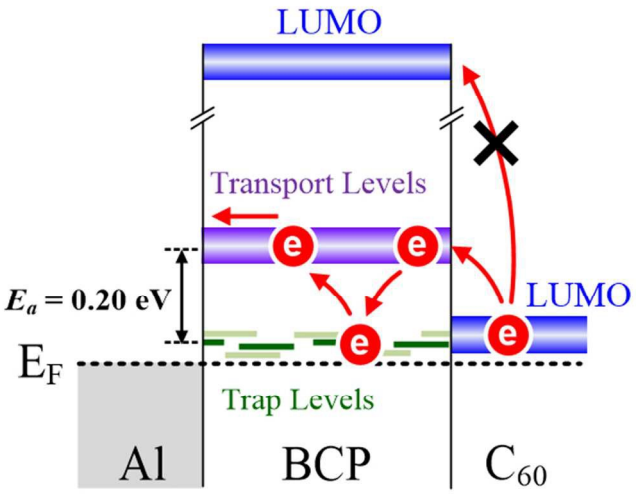

80x39mm (300 x 300 DPI)